

Timing accuracy of the Swift X-Ray Telescope in WT mode

G. Cusumano¹, V. La Parola¹, M. Capalbi^{2,3}, M. Perri^{2,3}, A. P. Beardmore⁴, D. N. Burrows⁵, S. Campana⁶, J. A. Kennea⁵, J. P. Osborne⁴, B. Sbarufatti^{5,6}, G. Tagliaferri⁶

¹ INAF – Istituto di Astrofisica Spaziale e Fisica Cosmica di Palermo, Via U. La Malfa 153, 90146 Palermo, Italy

² ASI Science Data Center, Via G. Galilei, 00044 Frascati, Italy

³ INAF – Osservatorio Astronomico di Roma, via Frascati 33, 00040 Monteporzio Catone, Italy

⁴ Department of Physics and Astronomy, University of Leicester, University Road, Leicester LE1 7RH, UK

⁵ Department of Astronomy and Astrophysics, The Pennsylvania State University, 525 Davey Laboratory, University Park, Pennsylvania 16802, USA

⁶ INAF – Osservatorio Astronomico di Brera, Via Bianchi 46, 23807 Merate, Italy

Preprint online version: August 22, 2018

ABSTRACT

Context. The X-Ray Telescope (XRT) on board Swift was mainly designed to provide detailed position, timing and spectroscopic information on Gamma-Ray Burst (GRB) afterglows. During the mission lifetime the fraction of observing time allocated to other types of source has been steadily increased.

Aims. In this paper, we report on the results of the in-flight calibration of the timing capabilities of the XRT in Windowed Timing read-out mode.

Methods. We use observations of the Crab pulsar to evaluate the accuracy of the pulse period determination by comparing the values obtained by the XRT timing analysis with the values derived from radio monitoring.

We also check the absolute time reconstruction measuring the phase position of the main peak in the Crab profile and comparing it both with the value reported in literature and with the result that we obtain from a simultaneous Rossi X-Ray Timing Explorer (RXTE) observation.

Results. We find that the accuracy in period determination for the Crab pulsar is of the order of a few picoseconds for the observation with the largest data time span. The absolute time reconstruction, measured using the position of the Crab main peak, shows that the main peak anticipates the phase of the position reported in literature for RXTE by $\sim 270 \mu\text{s}$ on average ($\sim 150 \mu\text{s}$ when data are reduced with the attitude file corrected with the UVOT data). The analysis of the simultaneous Swift-XRT and RXTE Proportional Counter Array (PCA) observations confirms that the XRT Crab profile leads the PCA profile by $\sim 200 \mu\text{s}$. The analysis of XRT Photodiode mode data and BAT event data shows a main peak position in good agreement with the RXTE, suggesting the discrepancy observed in XRT data in Windowed Timing mode is likely due to a systematic offset in the time assignment for this XRT read out mode.

Key words. X-rays: general - instrumentation: detectors - methods: data analysis - X-rays: individuals: PSR J0534+2200

1. Introduction

The Swift satellite (Gehrels et al. 2004), launched on 2004 Nov 20, was mainly designed to detect and localize gamma-ray bursts (GRBs), providing autonomous rapid-response observations and long-term monitoring of the afterglow emission in a broad energy band from UV/optical to X-rays. After 7 years of operation it has observed more than 600 GRBs, collecting a huge amount of prompt and afterglow data whose study has revolutionized our understanding of the GRB phenomenology. Besides GRBs, Swift has observed many other classes of cosmic source, dedicating a growing fraction of its observing time to the so called “secondary” science.

The Swift payload includes three instruments: the Burst Alert Telescope (BAT; Barthelmy et al. 2005) observing in the 15–350 keV band, the X-Ray Telescope (XRT; Burrows et al. 2005) with an energy range of 0.3–10 keV and the Ultra-Violet/Optical Telescope (UVOT; Roming et al. 2005) with a wavelength range of 170–650 nm. XRT is a focusing X-ray telescope based on grazing incidence Wolter I mirrors, equipped

with a single e2v CCD-22 detector at its focal plane. The XRT focal detector was designed to support four different data read-out modes (see Hill et al. 2004 for an exhaustive description) in order to cover a wide range of source intensities and to follow rapid variability of transient phenomena through an automatic transition among the read-out modes according to the intensity of the source. The Imaging read-out mode is used soon after the slew to a newly detected transient phenomenon to record a prompt image of the field of view for a rapid evaluation of the source coordinates, with no spectroscopy or time resolved data. The Photodiode mode (PD) was designed to observe very bright sources, up to 60 Crab, with no spatial information and to achieve a high timing resolution of 0.14 ms. This mode has been disabled following a micrometeorite hit on May 27, 2005 that produced a very high background rate due to hot pixels which cannot be avoided during read-out in this mode (Abbey et al. 2006). The Photon Counting mode preserves the full imaging and spectroscopic resolution but with limited time resolution (2.5 s). This operation mode is suitable for source fluxes below $\sim 1 \text{ mCrab}$.

Windowed Timing (WT) mode uses the central 200 columns of the CCD (corresponding to a 8 arcminutes wide detector strip)

Obs ID	T_{elapsed} (s)	Exposure (s)	snapshot #	T_{epoch} (TDB) (MJD)	P^a (ms)	ΔP^b (ms)	P_{Radio} (ms)	$P - P_{\text{radio}}$ (ms)
00050100007	6341.9	1079.6	2	53395.0964704775688	33.5724117	7.9×10^{-6}	33.5724126208	-0.8
00050100016	24218.2	7872.3	5	53454.2110966913096	33.5745613	2.2×10^{-6}	33.5745609884	0.3
00058970001	272341.0	14049.7	13	53685.5802279020791	33.5829830	1.4×10^{-6}	33.5829688914	14.1
00050100019	17910.7	2277.4	4	53804.1732743901957	33.5872787	3.8×10^{-6}	33.5872782420	0.5
00050100020	87377.5	6602.1	12	53842.4607787839923	33.5886667	2.4×10^{-6}	33.5886694548	-2.7
00050100021	23920.8	4068.7	5	54179.6713066744996	33.6009160	2.6×10^{-6}	33.6009213337	-5.3
00058990007	417.1	417.2	1	54180.8642858685562	33.6009330	1.5×10^{-5}	33.6009646766	-32.0
00050100025	47091.4	4408.4	6	54389.3152526219274	33.6085555	4.4×10^{-6}	33.6085374589	18.0
00050100026	86544.1	2188.6	10	54407.4404817774775	33.6091754	1.4×10^{-5}	33.6091959069	-20.4
00050100027	167615.6	2939.5	11	54408.9766301068885	33.6092231	1.4×10^{-5}	33.6092517043	-28.5
00050100028	183.0	183.0	1	54410.5885580012327	33.6092286	4.3×10^{-5}	33.6093102548	-81.6
00050100029	51788.6	664.6	10	54698.3010557031885	33.6197938	5.2×10^{-5}	33.6197609238	32.9
00050100030	52479.5	9384.8	10	54698.3067390939323	33.6197619	1.4×10^{-6}	33.6197611302	0.7
00058990008	34342.2	1961.8	3	54855.1593480434822	33.6254844	7.7×10^{-6}	33.6254579123	26.5
00058990009†	18154.6	2661.1	4	54860.8810891913527	33.6256511	9.6×10^{-6}	33.6256657087	-14.6
00058990010	35558.6	6188.7	7	55091.7671635479928	33.6340536	1.3×10^{-6}	33.6340503694	3.2
00058990011†	29024.1	1720.6	6	55221.3119214096732	33.6387293	1.1×10^{-5}	33.6387543790	-25.1
00058990013†	1043.0	1043.0	1	55226.2780278549253	33.6389076	7.4×10^{-6}	33.6389346895	-26.9
00030371002†	982.0	982.0	1	55461.7032943207232	33.6474857	1.9×10^{-6}	33.6474823886	3.2
00030371003†	4182.2	952.2	2	55462.8191109598702	33.6475174	5.5×10^{-6}	33.6475228989	-5.5
00030371004†	1012.0	682.6	2	55463.5876044134566	33.6475470	3.7×10^{-6}	33.6475507994	-3.8
00030371005†	975.8	975.8	1	55463.0517034763325	33.6475465	1.5×10^{-5}	33.6475313433	15.1
00030371006†	4170.3	958.8	2	55463.2863167333053	33.6475527	6.9×10^{-6}	33.6475398610	12.9
00030371007†	978.6	978.6	1	55463.8446768862923	33.6475631	5.6×10^{-6}	33.6475601325	2.9
00030371008†	6083.2	963.3	2	55464.1003792808988	33.6475533	5.3×10^{-6}	33.6475694159	-16.1
00030371012†	48177.7	4345.0	3	55465.3235006383620	33.6476146	5.1×10^{-6}	33.6476138216	0.8
00030371013†	70241.8	4996.4	4	55466.4693566183778	33.6476498	2.4×10^{-6}	33.6476554220	-5.7
00030371014†	23738.6	1902.4	2	55467.1899126402641	33.6476776	4.4×10^{-6}	33.6476815817	-4.0
00030371015†	1035.7	1035.7	1	55471.0121225304683	33.6478160	3.7×10^{-6}	33.6478203235	-4.3
00058990012†	955.1	955.1	1	55574.5999367492113	33.6515869	1.8×10^{-6}	33.6515809950	5.9
00030371016†	1818.7	1818.7	1	55663.7859681778500	33.6548202	1.8×10^{-5}	33.6548186029	1.6
00030371017†	983.7	983.7	1	55666.8520923440810	33.6549298	5.6×10^{-6}	33.6549299033	-0.1
00030371018†	989.8	989.8	1	55667.7889097694278	33.6549750	1.1×10^{-5}	33.6549639096	11.1
00030371019†	981.8	981.8	1	55668.6640721579242	33.6549899	5.6×10^{-6}	33.6549956777	-5.7
00030371020†	975.6	975.6	1	55669.5940489891800	33.6550312	3.7×10^{-6}	33.6550294354	1.8
00030371021†	1191.7	1191.7	1	55670.076337797928	33.6550446	5.6×10^{-6}	33.6550469423	-2.4
00030371023†	1440.6	1427.6	2	55671.2719624312667	33.6550879	5.6×10^{-6}	33.6550903427	-2.5
00030371024†	1289.2	1289.2	1	55672.8748742345924	33.6551479	5.6×10^{-6}	33.6551485270	-0.7
00050100031★	1017.8	1017.8	1	55776.9641634614309	33.6589272	3.7×10^{-6}	33.6589269212	0.3
00058990014†	319.7	319.7	1	55946.7126451355507	33.6650358	2.6×10^{-5}	33.6650883028	-52.4
00058990015†	1473.0	1473.0	1	55951.3198558431759	33.6652550	5.6×10^{-6}	33.6652555472	-0.5

Table 1. Observation log and period search results.

^a Best period obtained through the folding technique.

^b 68% confidence level error on the best period.

† Observations where an attitude file corrected by UVOT data is available.

★ Observation simultaneous with the RXTE-PCA observation.

and provides a one dimensional image by compressing them into a single row. The timing resolution achieved by the WT read-out mode is 1.7791 ms. This operation mode is suitable for source fluxes below ~ 1 mCrab. This mode is now used for bright sources and, among the presently operational XRT read-out modes, is the one with the best timing resolution.

In this paper we describe the in-flight timing calibration of the XRT WT mode, investigating the accuracy in the period search and the absolute timing through the analysis of the Crab pulsar data. The Crab pulsar (PSR J0534+2200) has been used for in-flight calibration for several X-ray telescopes (e.g. Kuster et al. 2002; Rots et al. 2004; Kirsch et al. 2004; Terada et al. 2008; Molkov et al. 2010) and it is continuously monitored in the radio with its ephemeris regularly updated on a monthly basis and made available by the Jodrell Bank Observatory¹. The shape of its pulse profile, with a prominent main peak whose position in X-rays (as measured by RXTE in the energy band 2–16 keV) leads the radio one by $344 \pm 40 \mu\text{s}$ (0.0102 ± 0.0012 in phase, Rots et al. 2004), is a useful tool to investigate the absolute timing performance of the XRT instrument.

The paper is organized as follows: Section 2 describes how time is assigned to photon events in WT mode; Section 3 summarizes the Crab pulsar observations, the reduction of the XRT data and of the Crab observation performed by RXTE simultaneously with XRT; Section 4 describes the timing analysis and reports the results; in Section 5 we give a brief discussion of the results.

2. Reconstruction of photon arrival times in WT mode

The XRT WT mode is a CCD read-out mode used to achieve high resolution timing (1.7791 ms) with 1-D position information along the detector X direction. In this mode only the central part of the CCD is used. Different “windows” can be set and for flight observations a 200 columns wide window (covering about 8 arcminutes) is being operated. The read-out data are generated by clocking 10 rows (parallel transfers) into the serial register, where the signal is summed, and then reading out the central 200 columns.

Because in this mode the CCD rows are clocked at a regular rate (instead of transferring charge into the store area and then reading it out, typical of the 2D frame transfer in PC mode),

¹ <http://www.jb.man.ac.uk/pulsar/crab.html>

there is no inherent frame structure to the data stream. For convenience, telemetry frames containing 600 serial read-out rows (each one containing ten CCD rows) are generated when formatting the data. For each frame the header includes, for the first and last row, the time at which the last pixel in the row was digitized. In the following these two time values are called Frame Start Time (FST) and Frame End Time (FET), respectively. The values of FST and FET are expressed in MET (Mission Elapsed Time since January 1, 2001, UTC) and stored in the columns 'FSTS', 'FSTSub', 'FETS' and 'FETSub' of the XRT Housekeeping Header Packets file with a time resolution of 20 μ s.

The temporal delays between the photon arrival times and the read-out times are calculated during the ground processing. This is done by a specific software module, named XRTTIMETAG which is part of the XRT Data Analysis Software (XRTDAS²).

The 'xrttimetag' task calculates the arrival time of each photon based on the number of row transfers and column shifts required to move that pixel from the row centered on the X-ray source (DETY) to the output register. More specifically, the photon arrival times (in MET) are reconstructed according to the following equation:

$$t_{ph} = FST + RAWY\Delta t_{row} - \Delta t - 0.5\Delta t_{row} \quad (1)$$

where RAWY is the frame row number (0,599). The Δt term is the transfer time to reach the output serial register taking into account the position of the pixel on the detector and the time needed to cross the frame store area which is composed of 602 rows. This term is given by:

$$\Delta t = int[(601+DETY)/10]\Delta t_{row} + [mod(601+DETY, 10)+1]\Delta t_p \quad (2)$$

where *int* indicates the integer part of the number included in the square brackets, *mod*(601 + DETY, 10) indicates the remainder of the division by ten, Δt_p is the time for a CCD row parallel transfer (15 μ s) and Δt_{row} (1.7791 ms) is the time interval to read a single row in the serial register:

$$\Delta t_{row} = (FET - FST)/599 \quad (3)$$

The term $0.5\Delta t_{row}$ is added to refer the time values calculated by XRTTIMETAG to the middle of the WT temporal bin (1.7791 ms).

The time-tagging algorithm requires for each pixel the knowledge of its DETY value, i.e. where in the detector Y direction that pixel was illuminated by the X-ray source as it crossed the CCD during the columns parallel transfers. In other words, it requires the knowledge of the location on the CCD of the X-ray celestial source. This information is not available in the telemetry data, which stores only 1-D positional information along the X direction (DETX). For this reason, the XRTTIMETAG module needs as inputs the sky coordinates (Right Ascension and Declination) of the pointed X-ray source. These sky coordinates are then used, together with the spacecraft attitude file, to calculate the corresponding DETY values as a function of time. The time tagging algorithm assumes that the field of view is dominated by a bright X-ray source, i.e. that every photon is registered on the CCD at the DETY position of this source. This assumption neglects the telescope PSF extension which introduces a temporal smearing.

For each XRT observation (respectless of the readout mode) the event arrival times in MET are stored in a FITS file where the two keywords MJDREFI and MJDREFF give the integer and the

fractional part of the reference time expressed in TT (Terrestrial Time). Since the spacecraft clock (set once soon after launch, and left free-running thereafter) is expected to drift with time, a correction factor is included in the keyword UTCFINIT that can be used to correct the time for the clock drift up to the start time of the observation. Furthermore, a finer correction that accounts also for the drift occurring during the observation can be achieved by using a full list of clock offsets that is periodically delivered by the Swift Mission Operation Center and used as input of the Solar System Barycenter (SSB) correction code BARYCORR³.

3. Observation and data reduction

We have analyzed all the Crab pulsar observations in the Swift archive performed with the XRT in WT mode and whose observing time interval is covered by a set of radio ephemerides provided by the Jodrell Bank Observatory. Observations where the Crab pulsar was more than 5 arcminutes off-axis were excluded from the analysis because the pulsar is at the edge or out of the WT image strip. Table 1 reports the details on the observations used for the analysis. The Level 1 data were downloaded from the HEASARC public data archive⁴ and calibrated, filtered and screened with the XRTDAS package included in the HEASoft 6.11 software release. Where possible, the observations were also reduced using the attitude file corrected with UVOT data⁵. This technique uses UVOT images to provide a more accurate attitude solution than can be achieved by the Swift star trackers. Hence it improves the accuracy of our knowledge of the source position on the XRT CCD, and hence the accuracy of the assignment of arrival times to the X-ray photons.

Events with grade 0–2 were selected for the analysis. The source events were extracted from each observation using a rectangular region with 40 pixel width centered on the pixel with higher intensity. This region allows us to select $\sim 94\%$ of the PSF of the Crab pulsar, which is located near the center of the Nebula. XRT arrival times were referred to the SSB using the Crab coordinates, RA = 05h 34m 31.972s Dec = 22° 00' 52".07 (Lyne et al. 1993), the JPL DE200 solar system ephemeris and the barycentric code BARYCORR, also transforming the time reference keywords into TDB. Due to the Swift low inclination equatorial orbit, and to the optimization strategy adopted for the pointing planning, each observation comes split into one to several pieces called snapshots with exposure times from a few hundreds of seconds to ~ 1 ks, separated by one or more orbits (each orbit lasts ~ 96 minutes).

The Crab pulsar was also observed on 2011 Aug 3 by RXTE (from 55776.95497588 to 55776.96972203 MJD, TDB time scale, Obs.ID 96802-01-12-00, with an exposure time of 915 s) following a request of the Swift-XRT hardware team for timing intercalibration. The time range of the RXTE observation was fully covered by the Swift-XRT observation (Obs ID 00050100031). We used data from the Proportional Counter Array (PCA, Bradt et al. 1993; Jahoda et al. 2006) collected in Event Mode, time-tagged with a 1 μ s accuracy with respect to the spacecraft clock, which is maintained to the TT time scale with an absolute time accuracy of a few μ s. Data from only four Proportional Counter Units and from all the layers were ana-

³ A full description of the time assignment in the Swift FITS files is available at http://swift.gsfc.nasa.gov/docs/swift/analysis/suppl_uguide/time_guide.html.

⁴ <http://heasarc.gsfc.nasa.gov/cgi-bin/W3Browse/swift.pl>

⁵ <http://heasarc.gsfc.nasa.gov/heasoft/ftools/headas/uvotattcorr.html>

² http://heasarc.gsfc.nasa.gov/docs/swift/analysis/xrt_swguide_v1_2.pdf

Obs ID	P_* ^a (ms)	ΔP_* ^b (ms)	$P_* - P_{radio}$ (ns)
00050100016	33.574560903	4.5×10^{-8}	-0.085
00058970001	33.582968895	3.4×10^{-9}	0.0036
00050100019	33.587278625	3.9×10^{-7}	0.38
00050100020	33.588669498	3.9×10^{-8}	0.043
00050100021	33.600921413	1.0×10^{-7}	0.08
00050100025	33.608537702	5.3×10^{-8}	0.24
80050100026	33.609195920	3.0×10^{-8}	0.01
00050100027	33.609251660	1.2×10^{-8}	-0.045
00050100029	33.619760953	1.2×10^{-7}	0.029
00050100030	33.619760862	5.5×10^{-8}	-0.27
00058990008	33.625457614	7.5×10^{-8}	-0.30
00058990009	33.625663868	3.5×10^{-7}	-1.8
00058990010	33.634050301	4.9×10^{-8}	-0.068
00058990011	33.638754348	8.0×10^{-8}	-0.031
00030371012	33.647613948	6.1×10^{-8}	0.12
00030371013	33.647655855	1.8×10^{-8}	0.43

Table 2. Results of the pulse phase analysis performed on the observations with at least 3 snapshots.

^a Best period obtained through the phase analysis technique.

^b 68% confidence level error on the best period.

lyzed (PCU0 was off). Data extraction was performed with the dedicated RXTE tools (HEASOFT v.6.11) and standard filtering criteria for obtaining the good-time intervals. We filtered the data using the 2–10 keV energy range in order to best match the Swift-XRT energy range. Photon arrival times were adjusted to the solar system barycenter using the same source position as for the Swift data, with the `FAXBARY` tool, applying the fine clock corrections.

4. Timing analysis and results

4.1. Accuracy of the Crab period estimation

For each observation we have derived the best Crab period with the following procedure:

1. We have applied a folding analysis (e.g. Lorimer et al. 2004) to the barycentered arrival times in each snapshot, fixing the folding epoch time to the observation central time (column 5 in Table 1), and searching in a period range centered on the expected period (column 8 in Table 1) evaluated using the Crab radio ephemeris. The period search was performed with a step resolution $\Delta P = P^2/(N\Delta T)$, where $N=100$ is the number of phase bins used to sample the pulse profile and ΔT is the data time span for each snapshot.
2. For each snapshot periodogram we derived the best period by fitting the χ^2 peak with a Gaussian function. The error on the best period (68% confidence level) was evaluated computing the period interval corresponding to a unit decrement with respect to the maximum in the χ^2 curve (Cusumano et al. 2003) i.e. $\Delta P = P(\chi_{max}^2) - P(\chi_{max}^2 - 1)$.
3. The best period for the whole observation (columns 6, 7 in Table 1) was obtained as the weighted mean of the best period values of the snapshots, using the errors on each period as weight.

Figure 1 (top panel) shows the best period values obtained for each observation vs. time and compares them with the ones derived from the radio ephemeris. The central panel shows the residuals with respect to the values extrapolated from the radio ephemeris (see also column 10 in Table 1). The folding analysis on these observations allows us to obtain an accuracy of the order of a few to tens of ns in the determination of the period,

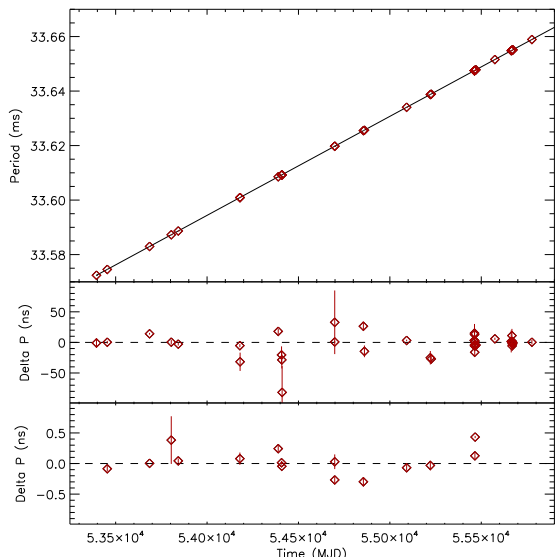


Fig. 1. Top panel: best periods obtained for each observation (column 6, Table 1) as weighted mean of the folding analysis results performed on single snapshots. The solid line connects the periods extrapolated at the folding epoch times from the radio ephemeris (column 8, Table 1). Central panel: residuals between the best periods plotted above and the corresponding periods as extrapolated from the radio ephemeris. Bottom panel: residuals between the periods obtained from the pulse phase analysis (column 2, Table 2) and those extrapolated from the radio ephemeris (column 8, Table 1). Due to the Y-axis range in the three panels, errors for several points are too small to be visible.

depending on the data time span and on the frequency of the snapshots within each observation.

The precision of the timing parameters can be enhanced by performing a pulse phase analysis on the observations with several snapshots (at least 3). This consists in maintaining a phase pulse coherence over the entire time interval covered by the observation. We have folded the event arrival times of each snapshot with the same epoch time used in the previous analysis and with the observation best period (column 6 in Table 1). Phase shifts of the pulse profile are expected because of the indetermination of the period within its error and of the presence of period derivatives. These phase shifts were evaluated by measuring the position of the main peak fitting it with a Lorentzian function plus a constant. The width of the Lorentzian was fixed to the value obtained in the observation with the highest statistics (ObsID 00058970001). As the main peak has an asymmetric shape, we checked for the presence of systematics in the determination of the peak position due to the choice of the model: fits with a Gaussian function and with a parabola agree within errors with the values obtained with the Lorentzian model, that were therefore used throughout the analysis.

In the absence of frequency irregularities (glitches), the correction to the frequency and its derivative can be obtained by fitting the phase lags by a third degree model:

$$\Delta\phi(t) = \Delta\nu_0(t - t_0) + \frac{1}{2}\Delta\dot{\nu}_0(t - t_0)^2 + \frac{1}{6}\Delta\ddot{\nu}_0(t - t_0)^3 \quad (4)$$

where $\Delta\phi$ is the measured phase difference at time t , t_0 is the epoch time, and $\Delta\nu_0$, $\Delta\dot{\nu}_0$, and $\Delta\ddot{\nu}_0$ are the correction to the frequency and to its first and second derivative, respectively. The

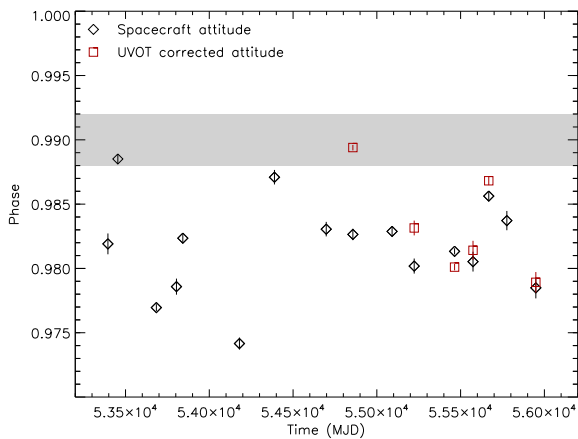


Fig. 2. Phase position of the Crab pulsar main peak (black diamonds). The shaded strip marks the phase range where the main peak is measured by RXTE-PCA. Red squares correspond to the phase position measured after correcting the attitude file with UVOT data. Observations with the same radio ephemeris sample interval were folded together and are thus represented by a single point.

data time span of the Crab observations is not long enough for the second derivative of the frequency to contribute significantly to the phase shift. Therefore the third degree term of the above polynomial is ignored in the fit. Table 2 reports the periods P_* (column 2) obtained applying $\Delta\nu_0$ from Eq. 4 to the periods reported in Table 1, and their associated errors ΔP_* (column 3) derived as $\sigma_{\Delta\nu_0} \times P_*^2$, where $\sigma_{\Delta\nu_0}$ is the 68% confidence level of $\Delta\nu_0$. Differences with respect to the periods extrapolated from the radio ephemeris are reported in column 4. The latter are also plotted in the bottom panel in Figure 1. The pulse phase analysis allows us to obtain an accuracy of the order of tens of picoseconds in the determination of the period, depending on the data time span, down to ~ 4 ps ($\Delta P/P \sim 10^{-9}$) for the observation with the longest time span (ObsID 00058970001). The accuracy on the estimate of the first derivative of the period depends both on the length of the data time span and on the number of snapshots; for ObsID 00058970001 we find a deviation of the period first derivative with respect to the value extrapolated from the radio ephemeris of 0.1%.

4.2. Absolute timing accuracy

The absolute timing of XRT in WT mode was evaluated measuring the phase position of the main pulse peak in the Crab profile obtained folding the XRT data with the radio ephemeris. Observations performed within the same radio ephemeris sample interval were folded together to improve the statistics of the pulse profile. As for the phase analysis, the phase of the main peak was then determined for each profile by fitting it with a Lorentzian function plus a constant. Figure 2 (black diamonds) shows the phase of the main peak vs. time, together with the range of values measured by RXTE (Rots et al. 2004). The positions of the main peak for each XRT observation are not consistent with each other and range between 0.9742 and 0.9885. The pulse profile leads the radio profile and also arrives systematically earlier with respect to the RXTE measure.

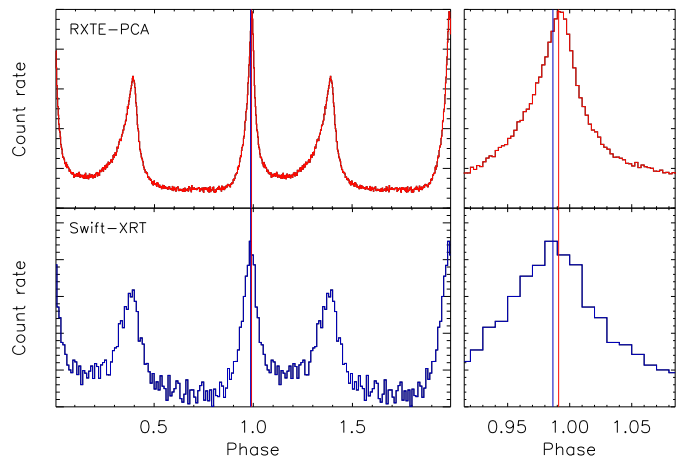


Fig. 3. Comparison between the Crab pulse profile obtained with RXTE-PCA (top panels) and that obtained with the Swift-XRT ObsID 00050100031. The count rates in the Y-axis are in arbitrary units. Vertical lines mark the position of the main peak (red: RXTE-PCA; blue: Swift-XRT). The right panels show a zoom of the main peak interval.

Instrument	Obs ID	T_{start} (TDB) (MJD)	$T_{elapsed}$ (s)	Exposure (s)
XRT-PD	00050100010	53396.14367194747	59153.3	15326.4
	00050100014	53399.01104749178	134287.2	29743.9
	00050101002	53414.08223807389	750.5	750.5
	00050102002	53414.15029296864	692.2	692.2
	00050101003	53426.60594507941	2333.8	2333.8
	00050101004	53437.05995839463	40799.0	3697.9
	00050100015	53442.21581378842	2354.5	2354.5
	00050100018	53470.36073094432	806.5	806.5
BAT	00050101001	53414.08275463	250.198	250.1
	00050101002	53414.08831019	250.189	250.1
	00050101003	53426.60660880	1250.255	1690.0
	00050102003	53438.00515046	100.20	23146.0
	00050100016	53454.07055556	1500.32	1500.3
	00050100021	54179.53190972	1727.93	13173.1
	00030371015	55471.00218500695	76.599	76.5
	00306746000	54544.09232639	696.857	1142.0
	00050100029	54698.00137482176	283.446	34621.8
	00058990008	54855.21901834028	293.189	11641.0
	00058990009	54860.77601602546	755.000	755.0
	00058990012	55574.59433546990	924.700	924.7
00050100031	55776.96256000000	970.165	970.1	

Table 3. XRT-PD and BAT Crab observations.

The average position of the main peak in XRT is at radio phase 0.9817 ± 0.0005 , corresponding to $\sim 620\mu\text{s}$ earlier than the radio peak and $\sim 270\mu\text{s}$ earlier than RXTE.

This analysis was also repeated for the observations reduced with the attitude file corrected with UVOT data (see Section 3 and first column in Table 1). Figure 2 (red squares) shows the result: the average values of the main peak phase is at 0.9854 ± 0.0002 , corresponding to $\sim 490\mu\text{s}$ earlier than the radio peak and $\sim 150\mu\text{s}$ earlier than RXTE, with a scatter ranging between 0.9801 and 0.9894.

The absolute phase was also verified using the RXTE observation performed simultaneously with Swift-XRT ObsID 00050100031 (for which only the spacecraft attitude file was available). Given their better time resolution, the RXTE data were folded using 400 phase bins. The XRT data were restricted to the energy range between 2 and 10 keV to better match the RXTE energy selection. The two pulse profiles, obtained folding the data with the radio ephemeris, are shown in Figure 3. The

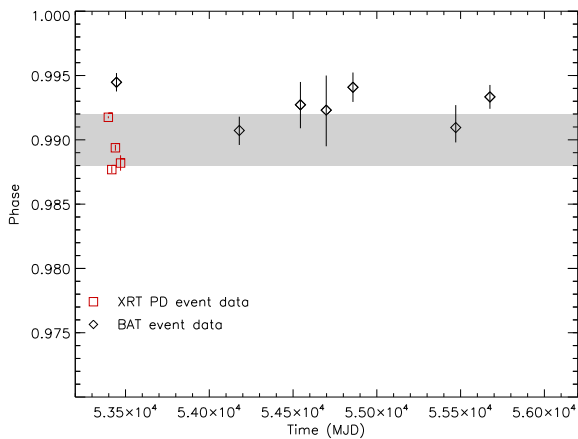


Fig. 4. Phase position of the Crab pulsar main peak for XRT-PD (red squares) and BAT (black diamonds) observations. The shaded strip marks the phase range where the main peak is measured by RXTE-PCA. For each instrument, observations with the same radio ephemeris sample interval were folded together and are thus represented by a single point.

comparison between the two profiles shows that the position of the main peak observed in XRT is earlier than the RXTE profile with an advance of $200 \pm 38 \mu\text{s}$. We have verified that the phase difference is not due to the different spectral content of the two datasets because of the different shape of the effective area in the two instruments: using the observation with the longest time data span (ObsID 00058970001) we do not observe any significant variation of the main peak phase when selecting in different energy range (2–10 keV, 4–10 keV, 6–10 keV, 8–10 keV). We have also verified that the phase difference is not due to the worse time resolution of the XRT dataset with respect to the RXTE one: we have modified the arrival times of the RXTE events by resampling them with a time resolution of 1.7791 ms and corrected them to the solar system barycenter; the resulting folded profile shows both a broadening ($\sim 35\%$) and a shift ($\sim 35 \mu\text{s}$ in advance) of the main peak. However, this shift is too small to account for the phase difference observed in the XRT profile.

We have checked if the difference in absolute timing observed between RXTE and XRT data in WT mode could also be observed in XRT data collected in PD mode (with $140 \mu\text{s}$ time resolution) and BAT data collected in event mode (with $100 \mu\text{s}$ time resolution). We have analyzed all Crab observations with suitable statistics available in the Swift archive. Table 3 reports the details on the observations used for this analysis. We selected PD data in the 2–10 keV range and BAT data in the 15–150 keV range. The barycentered data were analyzed using the same procedure as for the WT data, and the main peak positions obtained with a Lorentzian fit are plotted in Figure 4. The main peak position obtained by the pulse profiles of the PD mode data are fully consistent with the RXTE result; also for the BAT data we find a good agreement with RXTE. Moreover, for both data sets, the scattering is significantly smaller than that observed in XRT in WT mode.

5. Conclusions

We have analyzed the set of Swift-XRT Crab observations in order to qualify the timing performance of the XRT observing in WT mode.

The accuracy in the Crab period determination is mainly limited by the time span covered by the observation with a minimum difference of a few picoseconds with respect to the period extrapolated from radio ephemeris for the longest XRT observation.

We observe a displacement in phase of the Crab pulse profile with respect to the profile observed by RXTE-PCA: the main peak observed in XRT leads the RXTE-PCA one by $\sim 270 \mu\text{s}$ using the spacecraft attitude files, or $\sim 150 \mu\text{s}$ when UVOT corrected attitude files are available. This represents a 15% (9% using UVOT attitude files) shift in absolute timing compared to the time resolution of the XRT in WT mode. We have verified that this shift is not due to a spectral effect, nor to the worse time resolution of the XRT dataset with respect to the RXTE one. We observe a significant scatter in the position of the main peak among the XRT observations. Conversely, the peak positions obtained by the analysis of the Crab observations collected by XRT in PD mode and by BAT in event mode are in good agreement with the RXTE measurements. This suggests that the discrepancy observed in XRT WT mode is not due to the Swift spacecraft clock, but most likely to a systematic offset in the time assignment specific to this mode. However, the precision of the pulse period determination in WT mode suggests that the phase offset is stable within each observation even if it is not between observations.

Acknowledgements. The authors wish to thank the anonymous referee for critical review which allowed us to significantly improve the paper. APB and JPO acknowledge the support of the UK Space Agency. This work has been supported by ASI grant I/011/07/0.

References

- Abbey, T., Carpenter, J., Read, A., et al. 2006, *The X-ray Universe 2005*, 604, 943
- Barthelmy, S. D., Barbier, L. M., Cummings, J. R., et al. 2005, *Space Sci. Rev.*, 120, 143
- Bradt, H. V., Rothschild, R. E., & Swank, J. H. 1993, *A&AS*, 97, 355
- Burrows, D. N., Hill, J. E., Nousek, J. A., et al. 2005, *Space Sci. Rev.*, 120, 165
- Cusumano, G., Massaro, E., & Mineo, T. 2003, *A&A*, 402, 647
- Gehrels, N., Chincarini, G., Giommi, P., et al. 2004, *ApJ*, 611, 1005
- Hill, J. E., Burrows, D. N., Nousek, J. A., et al. 2004, *Proc. SPIE*, 5165, 217
- Jahoda, K., Markwardt, C. B., Radeva, Y., et al. 2006, *ApJS*, 163, 401 bibitem[Kirsch et al.(2004)]kirsch04 Kirsch, M. G. F., Becker, W., Benlloch-Garcia, S., et al. 2004, *Proc. SPIE*, 5165, 85
- Kirsch, M. G. F., Becker, W., Benlloch-Garcia, S., et al. 2004, *Proc. SPIE*, 5165, 85
- Kuster, M., Kendziorra, E., Benlloch, S., et al. 2002, arXiv:astro-ph/0203207
- Lorimer, D. R., Kramer, M., Ellis, R., et al. 2004, *Handbook of pulsar astronomy*, by D.R. Lorimer and M. Kramer. Cambridge observing handbooks for research astronomers, Vol. 4. Cambridge, UK: Cambridge University Press, 2004.
- Lyne, A. G., Pritchard, R. S., & Graham-Smith, F. 1993, *MNRAS*, 265, 1003
- Molkov, S., Jourdain, E., & Roques, J. P. 2010, *ApJ*, 708, 403
- Roming, P. W. A., Kennedy, T. E., Mason, K. O., et al. 2005, *Space Sci. Rev.*, 120, 95
- Rots, A. H., Jahoda, K., & Lyne, A. G. 2004, *ApJ*, 605, L129
- Terada, Y., Enoto, T., Miyawaki, R., et al. 2008, *PASJ*, 60, 25